

# Lawrence Berkeley National Laboratory

LBL Publications

## Title

Landslide monitoring using seismic refraction tomography — The importance of incorporating topographic variations

## Permalink

<https://escholarship.org/uc/item/4753f0v6>

## Authors

Whiteley, JS

Chambers, JE

Uhlemann, S

et al.

## Publication Date

2020-04-01

## DOI

10.1016/j.enggeo.2020.105525

Peer reviewed

1        **Landslide monitoring using seismic refraction tomography - The**  
2        **importance of incorporating topographic variations**

3        J S Whiteley<sup>1,2</sup>, J E Chambers<sup>1</sup>, S Uhlemann<sup>1,3</sup>, J Boyd<sup>1,4</sup>, M O Cimpoiasu<sup>1,5</sup>, J L  
4        Holmes<sup>1,6</sup>, C M Inauen<sup>1</sup>, A Watlet<sup>1</sup>, L R Hawley-Sibbett<sup>1,5</sup>, C Sujitapan<sup>2</sup>, R T Swift<sup>1,7</sup>  
5        and J M Kendall<sup>2</sup>

6        <sup>1</sup> British Geological Survey, Environmental Science Centre, Nicker Hill, Keyworth,  
7        Nottingham, NG12 5GG, United Kingdom. <sup>2</sup> School of Earth Sciences, University  
8        of Bristol, Wills Memorial Building, Queens Road, Bristol, BS8 1RJ, United  
9        Kingdom. <sup>3</sup> Lawrence Berkeley National Laboratory (LBNL), Earth and  
10        Environmental Sciences Area, 1 Cyclotron Road, Berkeley, CA 94720, United  
11        States of America. <sup>4</sup> Lancaster Environment Center (LEC), Lancaster University,  
12        Lancaster, LA1 4YQ, United Kingdom <sup>5</sup> Division of Agriculture and Environmental  
13        Science, School of Bioscience, University of Nottingham, Sutton Bonington,  
14        Leicestershire, LE12 5RD, United Kingdom <sup>6</sup> Queen's University Belfast, School of  
15        Natural and Built Environment, Stranmillis Road, Belfast, BT9 5AG, United  
16        Kingdom <sup>7</sup> University of Liege, Applied Geophysics, Department ArGEnCo,  
17        Engineering Faculty, B52, 4000 Liege, Belgium

18

19        Corresponding author: Jim Whiteley ([jim.whiteley@bristol.ac.uk](mailto:jim.whiteley@bristol.ac.uk))

20

21        Copyright British Geological Survey © UKRI 2020/ University of Bristol 2020

22

23 **Abstract**

24 Seismic refraction tomography provides images of the elastic properties of  
25 subsurface materials in landslide settings. Seismic velocities are sensitive to  
26 changes in moisture content, which is a triggering factor in the initiation of many  
27 landslides. However, the application of the method to long-term monitoring of  
28 landslides is rarely used, given the challenges in undertaking repeat surveys and  
29 in handling and minimizing the errors arising from processing time-lapse  
30 surveys. This work presents a simple method and workflow for producing a  
31 reliable time-series of inverted seismic velocity models. This method is tested  
32 using data acquired during a recent, novel, long-term seismic refraction  
33 monitoring campaign at an active landslide in the UK. Potential sources of error  
34 include those arising from inaccurate and inconsistent determination of first-  
35 arrival times, inaccurate receiver positioning, and selection of inappropriate  
36 inversion starting models. At our site, a comparative analysis of variations in  
37 seismic velocity to real-world variations in topography over time shows that  
38 topographic error alone can account for changes in seismic velocity of greater  
39 than  $\pm 10\%$  in a significant proportion (23%) of the data acquired. The seismic  
40 velocity variations arising from real material property changes at the near-  
41 surface of the landslide, linked to other sources of environmental data, are  
42 demonstrated to be of a similar magnitude. Over the monitoring period we  
43 observe subtle variations in the bulk seismic velocity of the sliding layer that are  
44 demonstrably related to variations in moisture content. This highlights the need  
45 to incorporate accurate topographic information for each time-step in the  
46 monitoring time-series. The goal of the proposed workflow is to minimize the  
47 sources of potential errors, and to preserve the changes observed by real  
48 variations in the subsurface. Following the workflow produces spatially  
49 comparable, time-lapse velocity cross-sections formulated from disparate,  
50 discretely-acquired datasets. These practical steps aim to aid the use of the  
51 seismic refraction tomography method for the long-term monitoring of landslides  
52 prone to hydrological destabilization.

53 **Keywords**

54 seismic refraction, geophysical monitoring, active landslides, topographic  
55 change, hydrogeophysics

56

57 **1. Introduction**

58 The implementation of robust and appropriate monitoring strategies is critical for  
 59 the ongoing assessment of potentially destabilising processes in landslide  
 60 systems (Angeli et al., 2000). Near-surface geophysical methods are increasingly  
 61 used to monitor the subsurface conditions of landslides susceptible to  
 62 hydrological destabilization (Perrone et al., 2014, Whiteley et al., 2019), most  
 63 commonly by active-source DC electrical resistivity (ER) (e.g., Lucas et al., 2017,  
 64 Uhlemann et al., 2017) and passive-source seismic monitoring (e.g., Walter et  
 65 al., 2012). ER can provide information on the moisture dynamics of an unstable  
 66 slope, and passive-source seismic can provide information on the kinematics of  
 67 failure events. One major advantage of active-source geophysical methods, such  
 68 as ER, is their ability to produce spatially high-resolution, time-lapse tomographic  
 69 images of the subsurface. However, the majority of seismic landslide monitoring  
 70 campaigns utilise passive-source methods, which provide superior temporal  
 71 resolution, but are limited in their spatial resolution due to practical limitations  
 72 on the number of sensors in an array.

73 Seismic refraction tomography (SRT), an active-source seismic method, can  
 74 characterize the spatial heterogeneities in elastic properties of materials in  
 75 landslide systems (e.g., Uhlemann et al., 2016). SRT determines the travel-time  
 76 of artificially generated seismic waves, to build up a series of travel-times for  
 77 waves propagating through the subsurface. These travel-times are inverted to  
 78 produce subsurface models of seismic velocity. The two types of body waves  
 79 used in SRT, P-waves and S-waves, propagate through subsurface media at  
 80 different speeds depending on lithological and physical properties. The P-wave  
 81 velocity,  $V_p$ , is given by

$$82 \quad V_p = \sqrt{\frac{K + \frac{4}{3}G}{\rho}}, \quad (1)$$

83 in which  $K$  is the bulk modulus (a measure of a material's resistance to uniform  
 84 compression),  $G$  is the shear modulus (a measure of a material's resistance to  
 85 shear strain) and  $\rho$  is material density. The S-wave velocity,  $V_s$ , is given by

$$86 \quad V_s = \sqrt{\frac{G}{\rho}}. \quad (2)$$

87 In solid rock, the relationship between seismic velocity and saturation has been  
88 empirically demonstrated, and is relatively well understood. Considering a fully  
89 saturated rock, as liquid (with a higher  $K$ ; Equation 1) in pore spaces initially  
90 become replaced by gas,  $V_p$  decreases rapidly and  $V_s$  decreases with increased  
91 saturation due to changes in bulk density and shear modulus (Equation 2) (Wyllie  
92 et al., 1956). These seismic attributes and their relationship to the petrophysical  
93 properties of rock can be used to determine the effects of saturation on seismic  
94 velocity (e.g., Biot, 1956, Gassmann, 1951).

95 In soils, the effect of variations in saturation on seismic velocity is less well-  
96 understood. Existing evidence indicates that both the distribution of moisture  
97 throughout the soil structure, as well as the influence that capillary forces have  
98 on effective pressure, influence  $V_p$  at small scales (Romero-Ruiz et al., 2018).  
99 Experiments in artificial, well-mixed, homogenous soils, have demonstrated that  
100  $V_p$  decreases with increasing saturation (Lu and Sabatier, 2009) and similar  
101 results have been obtained from laboratory measurements on undisturbed  
102 samples of Loess soils (Flammer et al., 2001). These decreases in  $V_p$  are  
103 dominated by changes in the matric potential of the soil (related to capillary  
104 forces). The effects of capillary forces are likely to be very different between  
105 artificial and natural soils, with the former having no internal structure or little  
106 consolidation, both of which reduce the influence of capillary forces.

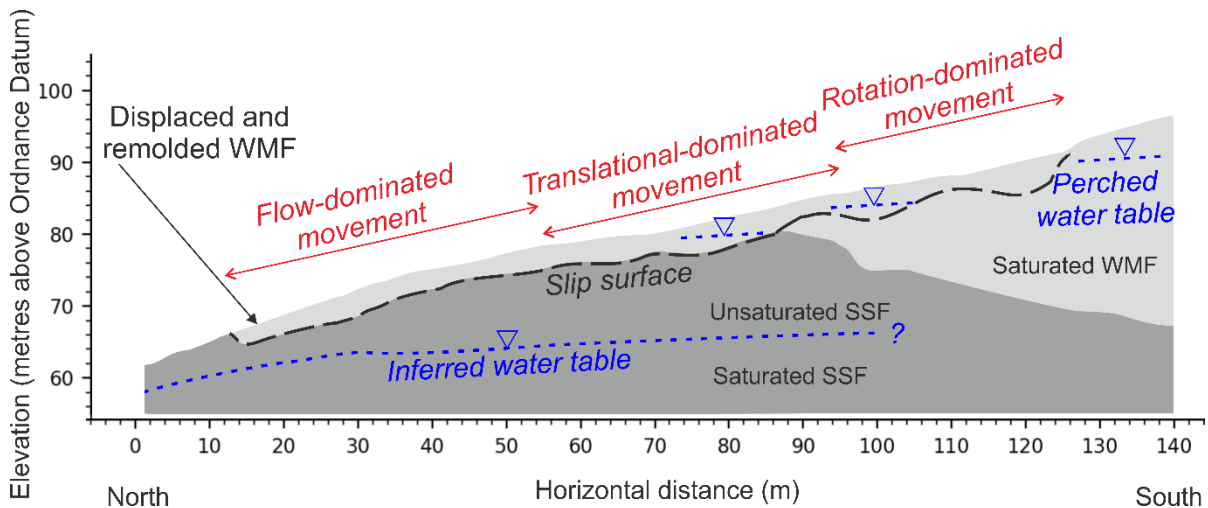
107 Despite this lack of understanding on the precise mechanism by which seismic  
108 velocities are influenced by moisture content in soils, seismic attributes are still  
109 routinely used in larger scale field studies to assess characteristics of near-  
110 surface sediments. The ratio between  $V_p$  and  $V_s$  ( $V_p/V_s$ ) can be used to assess  
111 lithology, strength and quality, structure and saturation of near-surface  
112 sediments for geotechnical investigations (Bhowmick, 2017). Seismic surveys to  
113 obtain in-situ  $V_p$ ,  $V_s$  and  $V_p/V_s$  have been used to image physical properties,  
114 including ground saturation, in the field (Dashwood et al., 2019, Pasquet et al.,  
115 2016b), and have been used to monitor shallow saturation processes in the  
116 laboratory (Pasquet et al., 2016a). Poisson's ratio, a property closely related to  
117  $V_p/V_s$  ratio which measures lateral strain to axial strain, has been shown to relate  
118 to porosity in near-surface sediments, and can be used to determine areas of  
119 localised saturation (Uhlemann et al., 2016, Uyanık, 2011).

120 The use of SRT as a tool for long-term landslide monitoring is almost absent from  
121 the literature. Examples of active-source seismic landslide monitoring campaigns

122 focus on the characterization of surface fissures (see Bièvre et al., 2012,  
123 Grandjean et al., 2009) rather than the monitoring of moisture-induced elastic  
124 property variations. The dearth of studies using SRT as a long-term monitoring  
125 tool for landslides is likely due to the complexity of managing and minimizing the  
126 several sources of error in the individual surveys (i.e., time-steps) that comprise  
127 a monitoring time-series. In this study, we present a methodology to acquire,  
128 process and invert a long-term SRT time-lapse dataset collected from an active  
129 landslide. To our knowledge, the use of SRT in a monitoring campaign at an  
130 active landslide site has not previously been implemented. The methodology is  
131 applied to time-lapse SRT monitoring at a site of active slope failure in North  
132 Yorkshire in the UK. This study aims to develop a practical approach for active-  
133 source time-lapse seismic surveying of vulnerable slopes, and to demonstrate  
134 the applicability of high spatial resolution subsurface monitoring using SRT. The  
135 approach taken is summarised in a workflow, from which a practical walkthrough  
136 of how the time-lapse SRT data were acquired, processed and inverted using a  
137 novel two-stage inversion procedure is presented. The importance of  
138 incorporating the topography of the landslide surface from every survey (i.e., for  
139 each time-step) in a monitoring campaign is highlighted. Summary results from  
140 the SRT monitoring campaign are presented and discussed, and support the use  
141 of SRT to monitor moisture dynamics at active landslide sites. The approach and  
142 results of this study should be of interest to researchers studying the evolution of  
143 subsurface processes acting to destabilise landslide systems (Jaboyedoff et al.,  
144 2019), and to those using geophysical methods in landslide early-warning  
145 systems (Intrieri et al., 2012) and monitoring environmental changes.

## 146 **2. Seismic refraction tomography monitoring at the Hollin Hill Landslide** 147 **Observatory**

148 The Hollin Hill Landslide Observatory (HHLO) in North Yorkshire, UK (Chambers et  
149 al., 2011, Merritt et al., 2013), is operated by the British Geological Survey. The  
150 landslide comprises an interbedded series of Lower and Middle Jurassic  
151 sandstones and mudstones (Figure 1), namely the Whitby Mudstone Formation  
152 (WMF) and Staithes Sandstone Formation (SSF).

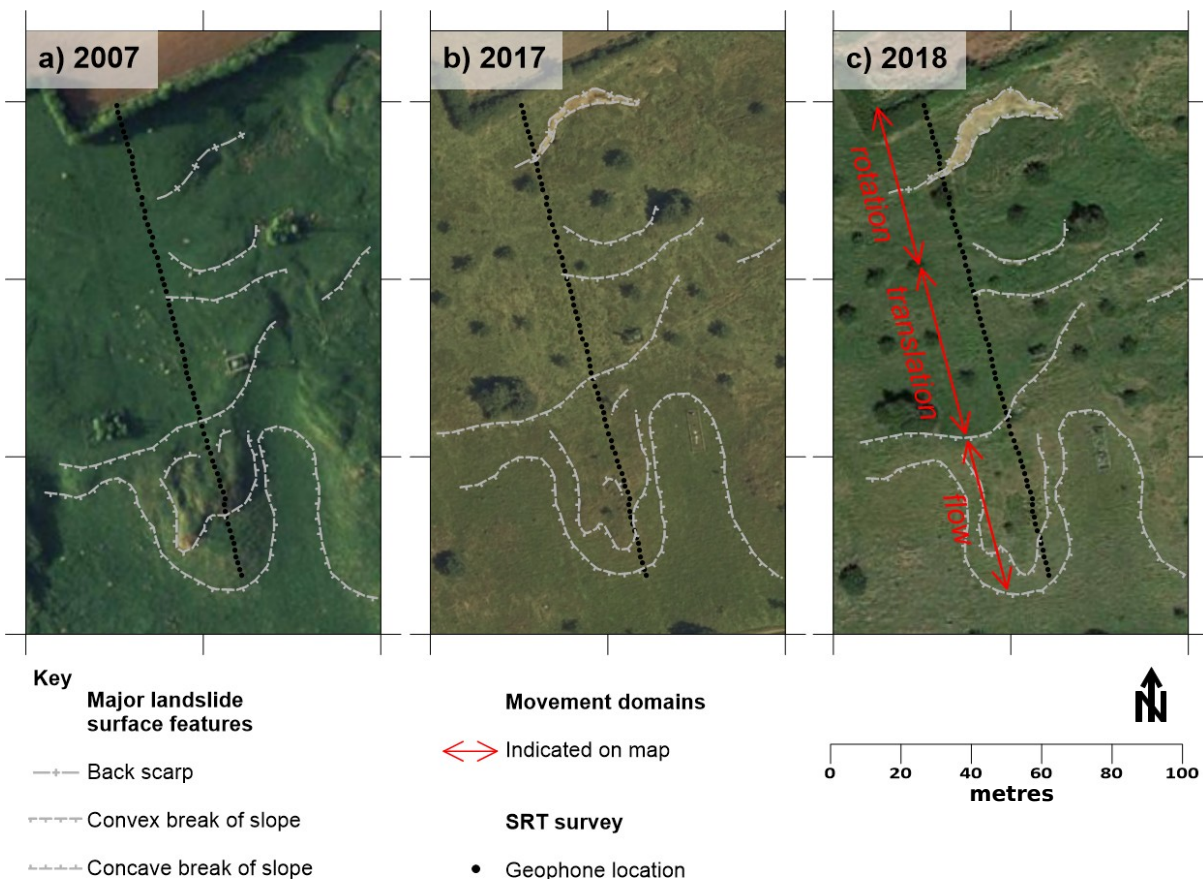


153

154 *Figure 1: A simplified conceptual model of the HHLO (modified from Uhlemann et al., 2016),*  
 155 *indicating movement domains, slip-surface, indicative position of water tables, and main lithological*  
 156 *units comprising the Whitby Mudstone Formation (WMF) and Staithes Sandstone Formation (SSF).*

157 The moisture content of the WMF controls displacement occurrence at the site.  
 158 The WMF is of low permeability and drains slowly into the underlying SSF. Hence,  
 159 during periods of increased precipitation, moisture content within the WMF  
 160 increases quickly (creating localized perched groundwater tables), and decreases  
 161 slowly during periods of lower precipitation. Slope failure is most likely during  
 162 these periods of intense and prolonged rainfall.

163



164 *Figure 2: Aerial photographs from the HHLO. a) Image from 2007 showing the main features of the*  
165 *landslide, including backscarps at top of slope (north), and flow-lobes at base of slope (south). Map*  
166 *data: Google, Infoterra Ltd and Bluesky. b) Image from 2017 showing development of new*  
167 *backscarp after movement in 2016. Map data: Digimap. c) Continued backscarp development*  
168 *shows landslide extension, and propagation of the backscarp to the west. Map data: Google. Black*  
169 *dots are the indicative locations of receivers used in the SRT surveys, with the first receiver*  
170 *location (northern most dot) located outside of the active landslide area, acting as a static*  
171 *reference point against which the receiver arrays are deployed. The location of this receiver is*  
172 *marked by a ground peg installed at the site.*

173 Seasonal variations in moisture content, linked to regional groundwater levels  
174 and local infiltration of rainwater, decrease restraining soil-suction forces  
175 (potentially producing destabilising positive pore-water pressures) initiating  
176 movement at the slip-surface mid-slope. This translational displacement  
177 propagates uphill as support for overlying material is removed, culminating in  
178 the development and widening of rotational backscarps in the saturated WMF at  
179 the top of the slope. Downslope, mobilised material is reworked to form flow  
180 lobes at the base of the landslide, where movement is eventually arrested  
181 through drainage to underlying deposits of well-sorted, aeolian quaternary sands  
182 deposited at the top of the SSF. Aerial imagery from 2007, 2017 and 2018 shows  
183 the development of geomorphological landslide features at the HHLO (Figure 2).

184 SRT monitoring at the HHLO aims to identify changes in the elastic properties of  
185 the underlying lithological units. These variations in elastic properties are  
186 primarily driven by variations in slope moisture dynamics. Between October  
187 2016 and August 2019, 16 SRT surveys were acquired, resulting in the  
188 production of 16  $V_p$  and 16  $V_s$  cross-sections spanning a period of 1001 days,  
189 close to 33 months. The length of time of the monitoring period allowed data to  
190 be collected over two distinct annual climatic cycles, ensuring data were  
191 acquired at different subsurface moisture contents, and during multiple wetting  
192 and drying phases of the landslide system, capturing temporal heterogeneity in  
193 hydrological condition. Data were acquired at an average return interval of 9  
194 weeks, which was deemed to be practicable given the characteristics of the  
195 landslide system and long-term monitoring period. A shorter return interval  
196 would have been desirable, but this was prevented by the logistical and financial  
197 cost of mobilisation, equipment availability and deployment, and acquisition and  
198 processing time associated with each survey; surveys typically involved two to  
199 three days of fieldwork, followed by several days of data processing.

200 The SRT surveys were acquired along the same profile location over the duration  
201 of the monitoring campaign. The profile comprised of 2 m spaced geophones  
202 (i.e., receivers), positioned from the crest of the landslide to the toe (Figure 2).



203 The location of the survey profile was chosen based on previous geophysical  
204 surveys that have been undertaken at the site (see Uhlemann et al., 2016) and  
205 position of geotechnical sensors (see Merritt et al., 2013). For both the P- and S-  
206 wave surveys, a 48-channel ABEM Terraloc Mk6 was used to acquire seismic  
207 refraction data. To acquire contiguous data from the entire spread length (142 m  
208 total length, comprising 72 receiver locations), two separate 48 receiver (94 m  
209 long) profiles with a 46 m overlap between the surveys were acquired. Receivers  
210 used in both deployments were not moved between spread acquisitions, and  
211 repeat shots were undertaken so that the overlapping spreads could be  
212 processed as a single profile of data.

213 Vertical geophones with a dominant frequency of 8 Hz were used as receivers for  
214 the P-wave survey, and a 4 kg sledgehammer and horizontal steel plate were  
215 used as a source. At each shot location, data were recorded for 1 second, in  
216 order to acquire both refracted P-wave arrivals and surface wave data (these  
217 latter data are not described in this study). Shot records were stacked in the  
218 field, and the number of stacked shot records varied between surveys based on  
219 environmental conditions, such as wind speed and rain; a minimum of two stacks  
220 per location were acquired in optimal conditions (i.e., low or no wind and rain),  
221 and up to six stacks per location were acquired in poorer conditions.

222 For the S-wave survey, horizontal geophones with a dominant frequency of 14 Hz  
223 were used as the receivers, and a prism with  $\sim 45^\circ$  inclined face was used to  
224 generate S-waves in opposing polarisations, perpendicular to the orientation of  
225 the receiver profile (Uhlemann et al., 2016). Data were recorded for 0.5 seconds,  
226 and same-polarisation shot records were stacked, with a minimum of two  
227 stacked per receiver location saved in optimal survey conditions, and up to a  
228 maximum of six shot records per location saved in poor survey conditions.

229 In both surveys, geophones were buried to a depth of  $\sim 10$  cm below ground  
230 level in an attempt to isolate the receivers from aerial environmental noise, and  
231 to provide better coupling with the subsurface. Shots were acquired at every  
232 other receiver location (i.e., every 4 m) for the whole of the receiver spread,  
233 starting at the first receiver at the crest of the slope. It was not possible to  
234 acquire off-end shots at the top of the profile (i.e., before the first geophone) due  
235 to access restrictions. For the P-wave surveys, off-end shots at the end of the of  
236 the spread were acquired at 4m intervals beyond the penultimate receiver at the  
237 toe of the slope to a maximum off-end distance of 22 m beyond the last receiver

238 (i.e., 164m from the first receiver). For the S-wave surveys, off-end shots were  
 239 acquired at 10 m intervals to a distance of 20 m beyond the last receiver (i.e.,  
 240 162 m from the first receiver). For both surveys, the same shot locations were  
 241 used throughout the entire monitoring campaign, ensuring consistent spatial  
 242 coverage between surveys.

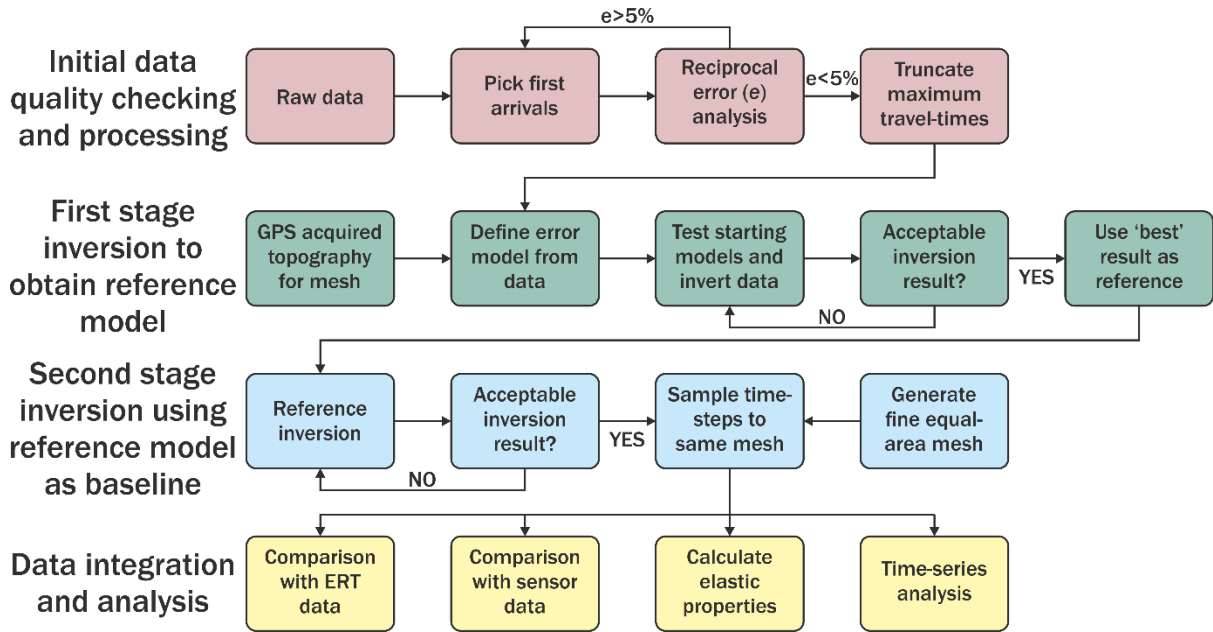
### 243 **3. Overcoming challenges in long-term SRT monitoring of landslides**

244 In this study, several sources of error in SRT surveys need to be accounted for  
 245 during data acquisition, and in the subsequent data processing and inversion  
 246 stages. Some of these sources of error are unique to landslide monitoring. The  
 247 goal during processing is to minimize transient changes in time-lapse data that  
 248 may arise from differences in survey set-up and processing of data between  
 249 surveys, and to preserve changes arising from genuine variations in the  
 250 properties of landslide materials. As velocity is the ratio of distance and time, the  
 251 determination of accurate velocities relies on accurate positioning (i.e.,  
 252 determining true distances) and correct picking (i.e., identifying correct travel-  
 253 times) of data. The major sources of potential error in SRT acquisition and  
 254 processing are identified in Table 1, along with their solutions presented in this  
 255 study and stage at which the error should be considered. A workflow to produce  
 256 a robust seismic velocity time-series, taking into consideration the potential  
 257 sources of error identified in Table 1, is shown in Figure 3. In this study, the 1001  
 258 day monitoring period is considered as a ‘time-series’ of SRT data, with the 16  
 259 individual surveys comprising ‘time-steps’ within this time-series. The following  
 260 sections describe how the stages of the workflow are used to address the  
 261 potential errors listed in Table 1 that occur within individual time-steps, and  
 262 across the time-series as a whole.

Potential source of error:	Addressed by use of:	Addressed during:
<b>Inconsistent repositioning of receivers to same locations between surveys</b>	Permanent reference points in the field for repeatable receiver deployment	Data acquisition
<b>Failure to capture accurate 3D locations of receivers deployments, and subsequent differences in positions between surveys</b>	RTK-GNSS systems to obtain accurate 3D receiver positions	Data acquisition
<b>Inconsistent data coverage within surveys and across the time-series</b>	Repeatable field procedures to boost data coverage; common travel-time maxima across time-series to give consistent data coverage	Data acquisition/ data processing
<b>Inconsistent picking of first arrivals</b>	Reciprocal error analysis to identify data for re-processing	Data processing
<b>Not accounting for changes in surface topography between</b>	Unique inversion for each survey (i.e., time-step) derived from individual RTK-	Data inversion

<b>surveys</b>	GNSS acquired topography	
<b>Not incorporating errors in to the inversion</b>	Error model derived from reciprocal error analysis	Data processing/ data inversion
<b>Using inappropriate constraints for initial data inversion</b>	Tests to determine best starting parameters for first stage inversion	Data inversion
<b>Using inappropriate constraints to regularize data over time</b>	Selecting 'best' data from first stage inversion to use as a 'reference model' for second stage of inversion	Data inversion

263 Table 1: Potential sources of error arising from the acquisition, processing and inversion of time-  
264 lapse SRT data.



265

266 Figure 3: Proposed workflow for processing SRT surveys (i.e., time-steps) to produce a reliable  
267 time-series of time-lapse SRT data. SRT data are first processed using reciprocal data analysis for  
268 quality control. Individual SRT survey data are initially inverted to determine the best time-step,  
269 from which the resulting model is then used as a 'reference model' for all the time-steps in the  
270 time-series. Time-lapse SRT images are then created using unique topography acquired at each  
271 survey, in order to determine velocity changes in the subsurface between surveys.

### 272 3.1. Assessing first arrival quality

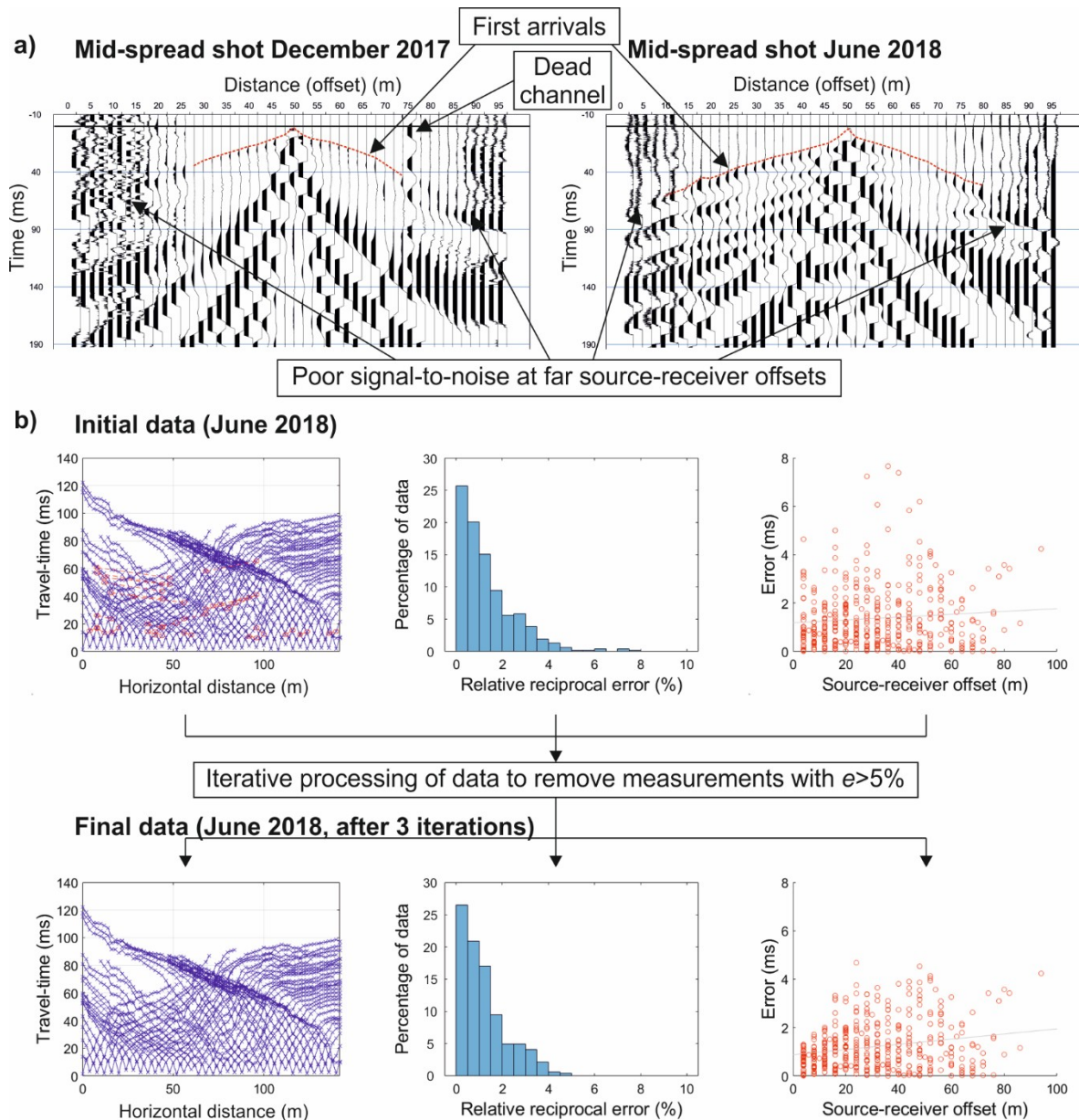
273 Identifying consistent, repeatable first arrivals in SRT data is a recognised  
274 challenge with no universally accepted solution. Attempts include using  
275 automatic picking algorithms (e.g., Khalaf et al., 2018) and using statistical  
276 approaches (e.g., Dangeard et al., 2018) to minimize absolute and relative errors  
277 introduced by operators picking time-lapse SRT data. In this study, reciprocal  
278 errors between inverse source-receiver configurations are used to identify 'bad'  
279 picks that display an unacceptable differential in reciprocal travel-time.  
280 Reciprocal measurements require receiver locations to be used as both receiver  
281 and source location during the course of the survey. Therefore, reciprocal  
282 analysis is undertaken on ~50% of the entire data for any given survey, and is  
283 used as a representative sample of the entire survey dataset i.e., a reciprocal

284 error subset. The error ( $e$ ) in a reciprocal measurement (defined as the mean  
285 travel-time of the two measurements) is defined as

$$286 \quad |e| = 100 \cdot \left( \frac{|t_n - t_r|}{t_n + t_r} \right),$$

287 (3)

288 in which  $t_n$  is the travel-time between a source at position A, and receiver at  
289 position B, and  $t_r$  is the travel-time between a source at position B and a receiver  
290 at position A. Reciprocal measurements cannot always be acquired when intra-  
291 survey (i.e., within the same time-step) data coverage is inconsistent. Factors  
292 leading to poor data coverage include low signal-to-noise-ratio at greater source-  
293 receiver offsets and interference from noise sources, such as wind, rain and  
294 amplification of these noise sources through nearby trees (Figure 4a). Large  
295 reciprocal errors occur in travel-times with greater source-receiver offsets, and  
296 therefore the use of reciprocal measurements as a data quality indicator favors  
297 data acquired from the very near-surface (i.e., shots with smaller source-receiver  
298 offsets). Across all of the reciprocal error subsets from each time-step in this  
299 study, 12.5% of the  $V_p$  data and 14.1% of the  $V_s$  data are not analyzed due to  
300 lack of reciprocal measurements. Remaining reciprocal-pairs of measurements  
301 showing a discrepancy  $e > 5\%$  are re-examined and re-picked (Figure 4b). Shot  
302 records adjacent to a reciprocal-pair with  $e > 5\%$  are also considered during this  
303 procedure. The data are then re-analyzed, and any further measurements with  
304  $e > 5\%$  are re-picked. This iterative process continues until all measurements in  
305 the dataset have  $e < 5\%$ .



306

307 *Figure 4: a) Examples of  $V_p$  shot records from the same position at the HHLO from December 2017*  
 308 *(left panel) and June 2018 (right panel). Poor signal-to-noise at larger source-receiver offsets*  
 309 *prohibits the identification of first arrivals, and prevents acquiring reciprocal pairs for every*  
 310 *measurement in the survey. b) The process of identifying reciprocal errors within a subset of the*  
 311 *refraction survey data with  $e > 5\%$  from  $V_p$  data from June 2017. Top left panel shows all first-arrival*  
 312 *data (displayed as travel-time curves) with pairs of measurements of  $e > 5\%$  circled in red. Top*  
 313 *centre panel shows the distribution of relative reciprocal errors within the reciprocal error data*  
 314 *subset, and the top right panel shows the distributions of absolute reciprocal errors from this data*  
 315 *subset as a function of source-receiver offset, indicating that shots with further offsets have higher*  
 316 *errors. The corresponding panels below show the effect of iteratively identifying and re-picking*  
 317 *data with  $e > 5\%$ , in order to reduce errors across the dataset.*

318 A further issue arising from implementing a time-lapse approach is achieving  
 319 consistent inter-survey (i.e., between time-steps) data coverage over time.  
 320 Consistent coverage cannot always be achieved due to variations in noise  
 321 sources and environmental factors between surveys. For example, surveys  
 322 undertaken in periods of increased ground moisture show higher signal

323 attenuation compared to surveys undertaken in drier conditions, and  
324 subsequently individual surveys show a significant variation in maximum  
325 recorded travel-times. Without normalization of these maximum travel-times,  
326 comparison of the inverted sections to determine an appropriate reference  
327 model (see Section 3.3) is challenging, primarily due to differences in maximum  
328 travel-times inducing significant variations in the maximum depths of coverage  
329 in the inverted models. To overcome this, the distribution of all travel-times from  
330 across the monitoring period is plotted, and a travel-time value that preserves  
331 the majority of the data is chosen as a cut-off. In this case, the chosen cut-off  
332 travel-times are 86 ms and 178 ms for the  $V_p$  and  $V_s$  data, respectively. Data with  
333 travel-times over this cut-off are discarded, creating consistency in coverage  
334 between time-steps, but reducing the total number of data points. Across all of  
335 the time-steps of this study, 1.5% of the  $V_p$  data and 17.1% of the  $V_s$  data are  
336 discarded, giving a common maximum travel-time between surveys. The  $V_s$   
337 surveys tend to have better signal-to-noise ratios, which results in a higher  
338 number of reliable first arrivals being recorded, however, this ultimately means  
339 that more data are discarded in order to match the relatively poorer coverage  
340 achieved in the  $V_p$  surveys.

### 341 **3.2. Using accurate topography**

342 Repositioning of receivers to repeatable  $x$ ,  $y$  and  $z$  positions on the landslide  
343 surface is crucial to ensure that seismic ray paths are sampling comparable  
344 domains of the subsurface over time. The positioning error in  $x$  and  $y$  can be  
345 minimized by deploying receivers relative to permanent markers located outside  
346 of the active area of the landslide, and recording absolute  $x$  and  $y$  positions for  
347 receiver locations. Furthermore, the slope surface ( $z$ ) will change between  
348 surveys. This effect cannot be removed by accurate positioning, and therefore  
349 needs to be incorporated into the data processing. Variations in  $z$ , as well as  
350 small unavoidable discrepancies in  $x$  and  $y$  positions can be captured using  
351 accurate geodetic surveying methods.

352 In this study, receivers are deployed every 2 m, with the first receiver located  
353 outside of the active landslide area (i.e., above the backscarp) and deployed at  
354 the same absolute position for each survey. A permanent ground peg marks the  
355 location of this first receiver, and a tape measure draped across the ground  
356 surface is used to deploy the remainder of the survey profile relative to this  
357 location. A Real-Time Kinetic Global Navigation Satellite System (RTK-GNSS) is

358 used to capture the absolute positions in  $x$ ,  $y$  and  $z$  of all receivers with a  
 359 precision  $<0.05$  m. With accurate positional data for each survey, the ‘line-of-  
 360 sight’ distance ( $d$ ) between one receiver location with coordinates  $(x_i, y_i, z_i)$  and  
 361 another with coordinates  $(x_{i-1}, y_{i-1}, z_{i-1})$  can be expressed as

$$362 \quad d_i = \sum_1^i \sqrt{(x_i - x_{i-1})^2 + (y_i - y_{i-1})^2 + (z_i - z_{i-1})^2} \quad . \quad (4)$$

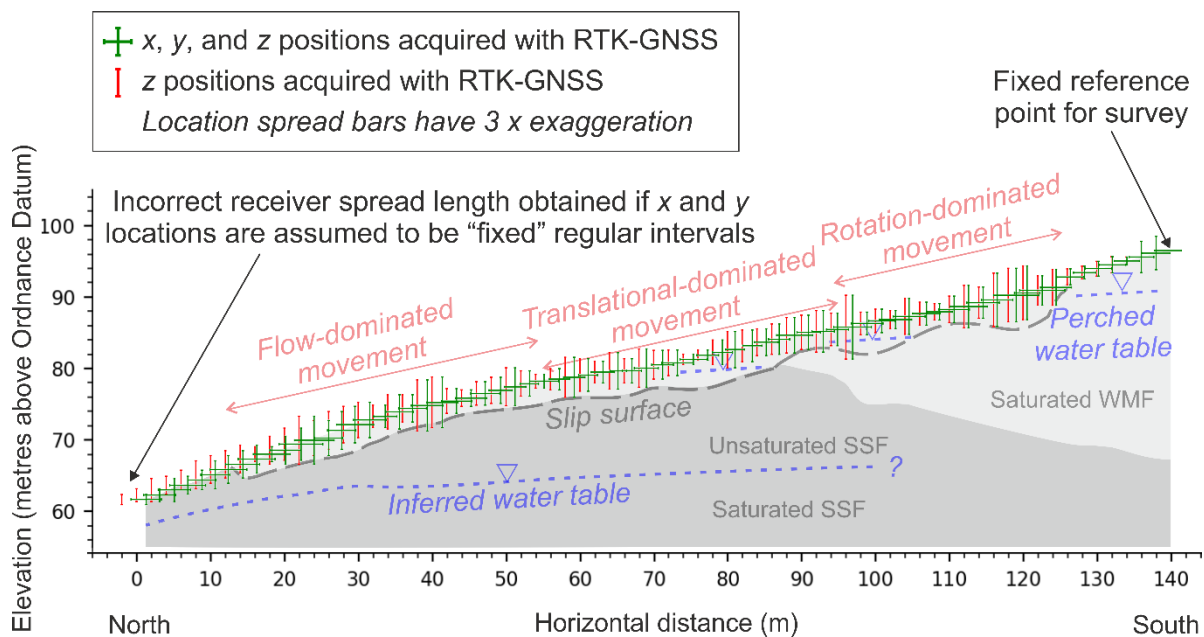
363 Topographic features between these receiver locations (i.e., those features  
 364 smaller than the receiver spacing) are not captured in the data.

365 For accurate 2D seismic travel-time inversion, accurate elevations and surface  
 366 distances of the receivers are required, as the fundamental problem to be solved  
 367 is one of distance and time. It is common in SRT surveys for the elevations ( $z_i$ ) of  
 368 sensors to be recorded accurately, but for the inter-receiver spacing to be  
 369 assumed to be a “fixed” nominal surface distance. This is particularly common in  
 370 surveys on flat or uniformly dipping surfaces, where accurate inter-receiver  
 371 spacing are easier to measure and control. However, in environments where  
 372 topography can vary sharply within the receiver array, such as landslides, this  
 373 approach can lead to errors in the positioning of receivers, which in turn  
 374 introduces errors in to the generation of subsurface meshes for inversion,  
 375 ultimately influencing the resulting inverted travel-times. Figure 5 shows the  
 376 discrepancies that can arise from assuming a “fixed” nominal spacing (e.g.,  
 377 assuming receivers are deployed every 2 m, without accounting for the changes  
 378 in distance that topography will create) with variable  $z_i$  measurements (red  
 379 points) against using the true  $x_i$ ,  $y_i$  and  $z_i$  positions to generate line-of-sight  
 380 distances using Equation 4 in this study (green points). Using a “fixed” nominal  
 381 spacing for time-lapse monitoring ignores lateral variations in receiver spacing,  
 382 and results in an overestimation of array length. Acquiring topographic  
 383 information at every survey (i.e., time-step) allows for accurate inversion of  
 384 travel-times.

385 At the HHLO, the SRT profile is orientated to match the maximum slope profile,  
 386 which is broadly parallel to the north-south orientation, and therefore the main  
 387 direction of recorded wave propagation for the SRT survey was also in a north-  
 388 south direction. Given the alignment of the  $y$  coordinate orientation with the  
 389 direction of wave propagation, greater variations in the  $y$  coordinate of the  
 390 receiver position (i.e., north-south orientation, parallel to slope) introduce larger

391 errors to the results of the seismic survey if not accounted for. Variations in x  
 392 coordinates (i.e., east-west orientation, perpendicular to slope) have a smaller  
 393 effect on measurement accuracy, as they are perpendicular to the wave  
 394 propagation direction. Between each survey, the mean variation in receiver  
 395 repositioning is 0.03 m in the x coordinate (1.5% of receiver spacing), and 0.01  
 396 m in the y coordinate (0.5% of receiver spacing), which is below the nominal  
 397 accuracy of the equipment used for data acquisition. Across the entire  
 398 monitoring period, receiver positions vary by an average of 0.41 m in the x  
 399 coordinate (20.5% of receiver spacing) and 0.15 m in the y coordinate (7.5% of  
 400 receiver spacing). The increased accuracy of deployment in the y coordinate is  
 401 due to the use of a tape measure deployed in the same orientation. Some active  
 402 areas of the landslide experience much greater variations in topographic change  
 403 due to slope displacements (Figure 5).

404



405

406 *Figure 5: The positions of receivers used in the SRT surveys at HHLO superimposed on to the site*  
 407 *conceptual model, and their variation over the monitoring period; the bars indicate the spread of*  
 408 *locations over the time-series (with 3 x exaggeration applied). The green points are surveyed*  
 409 *positions using an RTK-GNSS system, where Equation 4 has been used to generate true line-of-*  
 410 *sight receiver distances. The red points show how errors in positioning can arise if a “fixed”*  
 411 *nominal receiver spacing is assumed, resulting in lateral errors in receiver positions, and over-*  
 412 *estimation of slope length, which can result in inaccurate inverted seismic velocities.*

### 413 **3.3. Defining appropriate inversion parameters**

414 In this study, 2D inversion of the seismic data is undertaken using the open-  
 415 source Python based software *pyGIMLi* (Rücker *et al.*, 2017). This software allows  
 416 the inclusion of an error model fitted to the distribution of reciprocal errors



417 across the entire time-lapse dataset. A mesh-generation module in *pyGIMLi*  
 418 produces unique meshes for each time-step inversion, derived from the RTK-  
 419 GNSS measurements (see section 3.2). The production of unique meshes for  
 420 each time-step increases the accuracy of the model for each time-step, but  
 421 presents issues for later time-series analysis; in an ideal monitoring campaign,  
 422 the inversion meshes for each of the survey time-steps would be identical,  
 423 allowing for comparison of inverted velocity models on a cell-by-cell basis.  
 424 However, given the overriding importance of capturing the differences in  
 425 receiver positions and topography between time-steps, the use of unique  
 426 meshes is necessary, and this issue is addressed after the data inversion stage.

427 For this study, a two-stage ‘reference model’ inversion approach is used to  
 428 constrain the inversion and minimize differences between time-steps (Figure 3).  
 429 In the first stage, stand-alone inversions of all of the individual time-steps are  
 430 undertaken, with the aim of identifying the single time-step with the ‘best’  
 431 inverted model in terms of data fit. For this first-stage, it is necessary to define a  
 432 generic velocity gradient model (i.e., velocity increasing with depth) as the  
 433 starting model for the inversion process. In the first instance, we test the effects  
 434 of changing different parameters of the starting velocity gradient model by  
 435 changing these parameters and performing repeat inversions. The parameters  
 436 we test include the velocity bounds of the starting gradient model (i.e., velocity  
 437 at the surface and base of the model) and the maximum depth of the starting  
 438 model. From this process, we obtain a range of inverted models, and assess  
 439 which starting velocity gradient model parameters provide good results both in  
 440 terms of data-fit (by considering RMS and  $\chi^2$  values) but by also giving  
 441 consideration to our understanding of the subsurface based on the site  
 442 conceptual model (Figure 1). There is a risk that the inversion process will  
 443 introduce artefacts to improve data-fitting, and so qualitative comparison of  
 444 results with *a priori* site information is as equally important at this stage as  
 445 considering quantitative metrics of data-fitting. For this study, we are able to rely  
 446 on several sources of previous intrusive and geophysical data against which to  
 447 validate the inverted velocity model (see Chambers et al., 2011, Merritt et al.,  
 448 2013, Uhlemann et al., 2016, Uhlemann et al., 2017). Stand-alone inversions of  
 449 each time-step are performed using the parameters for the starting velocity  
 450 gradient model shown in Table 2.

Inversion settings							
Inversi	Dept	Minim	Maxim	Smoot	Maxim	Absol	Relat

Parameter	h of mesh	um velocity at surface	um velocity at base	hing factor (lambda)	um travel time	ute data error	ive data error
P-wave inversion input value	40 m	300 m/s	3000 m/s	25	86 ms	0.0242 ms	0.02 %
S-wave inversion input value	40m	100	1500	25	178 ms	0.0194 ms	0.006 %

451 Table 2: The optimal parameters for the starting velocity gradient model used in the first-stage  
452 inversion. These were obtained by changing their values and observing their effects on the  
453 inverted model output in terms of both data fit and comparison with the site conceptual model.  
454 Parameter values resulting in the 'best-fit' model were then used to invert all of the time steps, in  
455 order to identify the 'best-fit' model used for the second-stage of inversion.

456 RMS and  $\chi^2$  values are calculated for each inverted time-step model. The 'best-fit'  
457 model is assessed by looking at the divergence of  $\chi^2$  from a 'perfect-fit' model, in  
458 which  $\chi^2 = 1$ . The model with the lowest absolute divergence (i.e., closest to  $\chi^2 =$   
459 1) is designated as the 'reference model' for the second inversion stage. As no  
460 modelling error is included in the inversion, inversions do not typically converge  
461 at  $\chi^2 = 1$ . Details of the values of  $\chi^2$  and divergence from  $\chi^2$  for each inversion  
462 are shown in (see Table 3, in Appendix). From here, a single model is identified  
463 as having the 'best' fit and is taken forward to the second stage; all other  
464 resulting inverted models computed up to this stage are discarded.

465 In the second stage of the inversion process, the inversion of the entire data set  
466 is then repeated, but this time using the 'reference model' (i.e., the 'best' fit  
467 model) from stage one as the starting model. Using this method provides all of  
468 the time-steps a realistic and common starting model that is appropriately  
469 constrained and represents the local subsurface seismic properties. Within this  
470 second stage of the inversion, a nearest-neighbour lookup function allows the  
471 starting model to be sampled from the 'reference model' mesh to the inversion  
472 mesh, overcoming issues of topographic variance encountered by using different  
473 topography for mesh generation at each time-step. The result is a time-series of  
474 inverted seismic velocity models, all inverted using a common, real-world  
475 derived starting model.

476 As a result of incorporating unique topography for each time-step, each time-  
477 step uses a different mesh structure. To allow for consistent analysis of inverted  
478 velocity models between time-steps, the models are re-sampled and

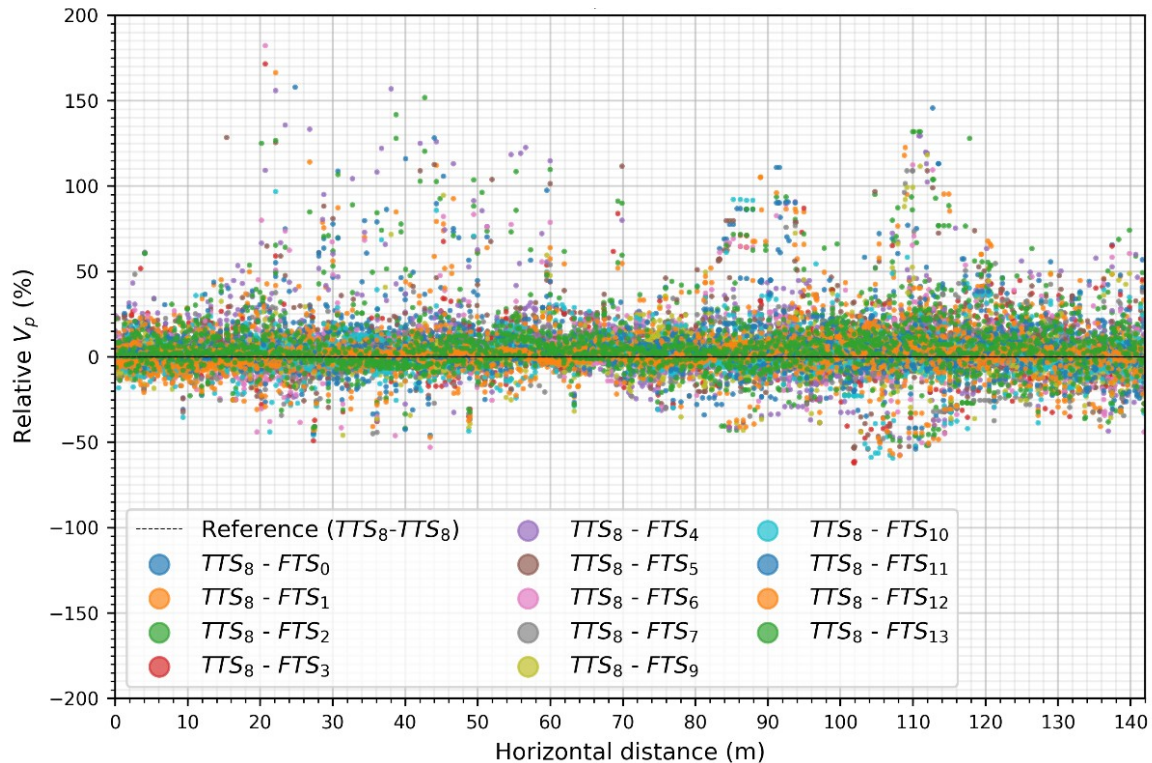
479 interpolated to a regular, refined, triangular mesh (constructed using the same  
480 *pyGIMLi* module), effectively creating a spatially-identical time-series on a  
481 consistent mesh (Figure 7a). We use a mesh generated with the most recent  
482 topography in the monitoring campaign, in order to better reflect an up to date  
483 state of the system. One consequence of this approach is that some cells from  
484 earlier surveys, in which the surface positions may now have slipped downslope  
485 are not sampled to the resampling mesh. To mitigate against this effect, we use  
486 a refined cell size that is smaller than the original cells used for the inversion,  
487 purposefully oversampling the inverted data in order to discretize the  
488 subsurface, and capture variations in the very near-surface. This enables a range  
489 of analyses of the time-lapse dataset (see Figure 3; Data analysis and  
490 integration).

#### 491 **4. Topographic induced variations in seismic velocity**

492 In section 3.2, we emphasise the importance of accurately capturing the intra-  
493 survey topography by using 2D line-of-sight distances from 3D GNSS surveys,  
494 and using topography data acquired for each individual survey in the monitoring  
495 campaign. This short section serves to demonstrate how failing to accurately  
496 capture variations in topography can have a significant impact on final inverted  
497  $V_p$  and  $V_s$  measurements.

498 To demonstrate the effect of temporal topographic variation on seismic velocity,  
499 the first 14  $V_p$  datasets ( $D_0:D_{13}$ ) and accompanying topographic surveys ( $T_0:T_{13}$ )  
500 are processed according to the workflow in Figure 3, and the text in Sections 3.1  
501 to 3.3. A P-wave travel-time dataset from midway through the monitoring  
502 campaign, January 2018 ( $D_8$ ), is processed and inverted using the surveyed  
503 topography ( $T_8$ ) to produce a 'true' time-step dataset ( $TTS_8$ ) comprising 2128  
504 subsurface  $V_p$  model points. The same seismic dataset ( $D_8$ ) is then processed  
505 using the remaining topographic data in the time-series ( $T_0:T_7, T_9:T_{13}$ ), resulting in  
506 13 SRT time-steps with 'false' topography ( $FTS_0:FTS_7, FTS_9:FTS_{13}$ ). The variations  
507 present in these 'false' time-steps represent the effect that real-world variations  
508 in topography across the monitoring period have on seismic velocity. By  
509 normalising all of the time-step data to  $TTS_8$ , the results from January 2018  
510 become a baseline against which variations in seismic velocity arising from  
511 subtle, but realistic changes in landslide topography are assessed. The result of  
512 this analysis is shown in Figure 6. They indicate that topographic variations can  
513 have a large impact on the resulting  $V_p$ , with 23% of the total data showing

514 velocities greater than  $\pm 10\%$  of the true maximum recorded velocity. This has  
 515 significant implications when trying to identify variations arising from genuine  
 516 subsurface elastic property changes caused by environmental factors, as these  
 517 variations can be very subtle (see Section 5).



518

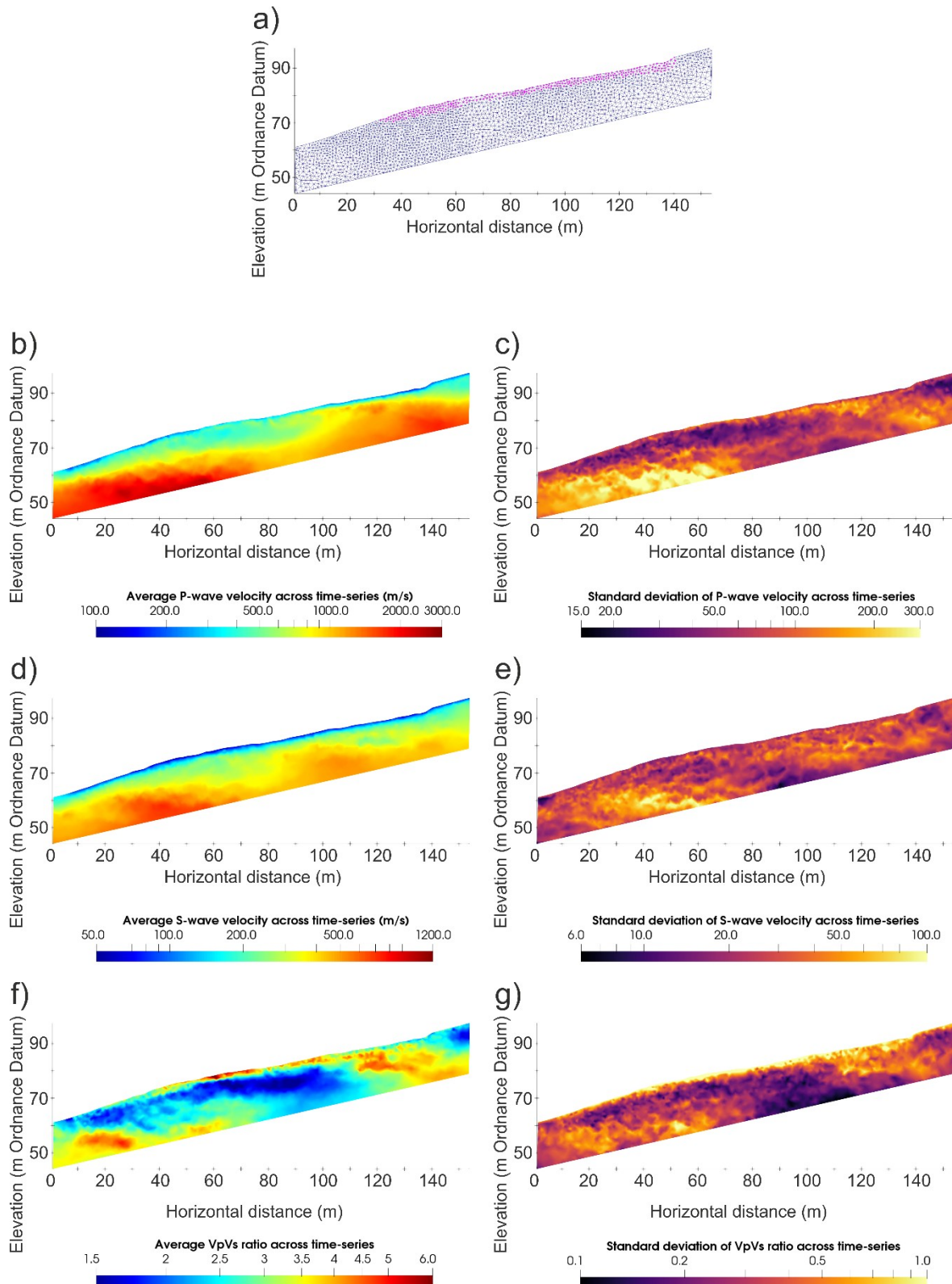
519 *Figure 6: Relative changes in  $V_p$  caused by subtle, real-world changes in topography. The solid*  
 520 *black line at  $y=0$  represents a normalised baseline ( $TTS_8 - TTS_8$ ). The same seismic dataset ( $D_8$ ) has*  
 521 *been processed using the other time-step topographic data; any variations in  $V_p$  are therefore a*  
 522 *product of these subtle topographic changes between surveys.*

## 523 **5. Data analysis and results**

524 One approach to analysing time-series SRT data is to look at how the seismic  
 525 attributes of discrete seismic units respond to changing environmental  
 526 conditions. The prevalent subsurface lithological discontinuities (i.e., those that  
 527 are stable in time) are highlighted by plotting the mean values of the individual  
 528 cells across the 33 month monitoring period (Figure 7). These plots are displayed  
 529 using the most recent topography in the time-series. The individual cross-  
 530 sections highlight significant subsurface features, including changes in lithology  
 531 at depth, and different domains of movement in the near surface. Plots showing  
 532 the standard deviation of these mean values (Figure 7) indicate the areas of the  
 533 landslide that show greatest velocity variation across the monitoring period.

534 Here we concentrate on the sliding layer at the HHLO (extending from the  
 535 surface to 2 - 4 m depth), which is easily identified by the low  $V_p$  and  $V_s$  at the

536 surface of the cross-sections. This extends from beneath the break in slope at  
537 the bottom of the back scarp (~15 m horizontal distance), to the base of the flow  
538 lobes (125 m horizontal distance). At HHLO this surface sliding layer is monitored  
539 by several subsurface and surface environmental sensors, recording rainfall and  
540 changes in moisture content, allowing direct comparison with inverted cross  
541 sections. By selecting grid cells within this layer, it is possible to calculate the  
542 change in velocity over time. In our case, the surface layer comprises model cells  
543 from both the  $V_p$  and  $V_s$  time-series datasets (Figure 7b and Figure 7d), the  
544 positions of which are



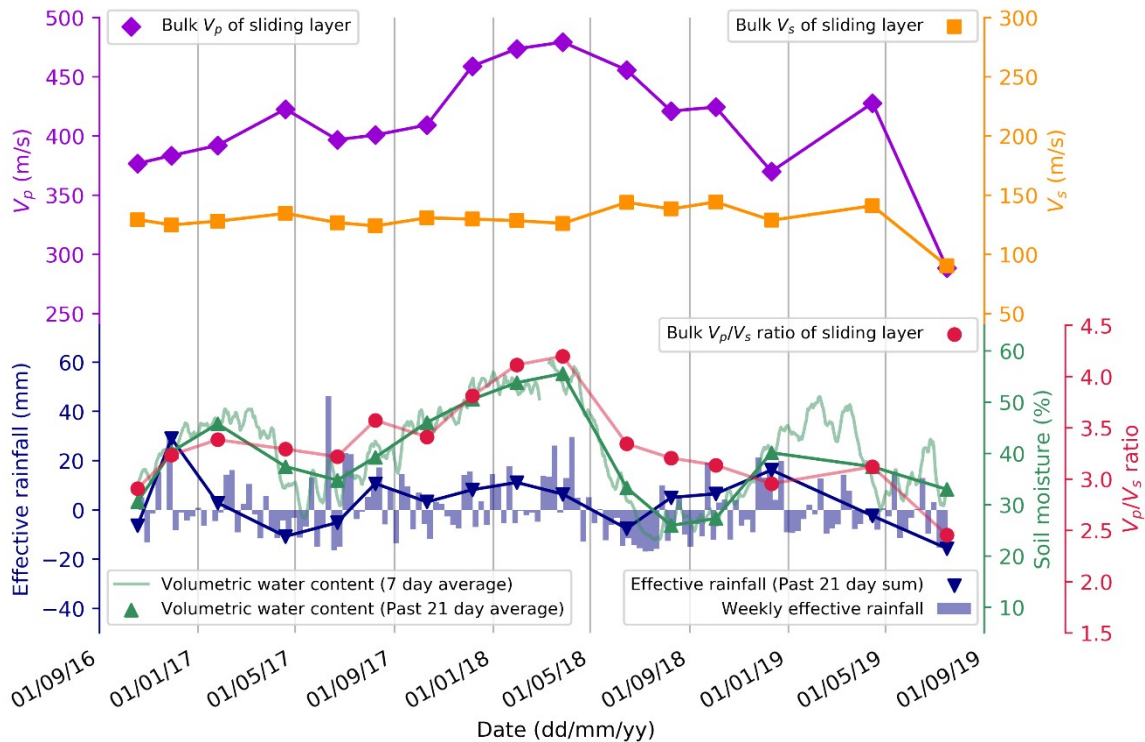
545

546 *Figure 7: a) The regular mesh used to sample all of the individual time-steps to create spatially*  
 547 *comparable datasets for the time-series. The cells highlighted purple in the surface sliding*  
 548 *have been used for the analysis in Figure 8. b) Cross-section showing average  $V_p$  across the time-series.*  
 549 *The value shown in each cell (see Figure 7a) is the mean velocity value from the entire 33 month*  
 550 *monitoring period. c) Cross-section showing average  $V_s$  across the time-series. The value shown in*  
 551 *each cell (see Figure 7a) is the mean velocity value from the entire 33 month monitoring period. d)*

552 *Cross-section showing average  $V_p$ ,  $V_s$  across the time-series. The value shown in each cell (see*  
553 *Figure 7a) is the mean ratio value from the entire 33 month monitoring period.*

554 fixed through the use of a common fixed mesh. Figure 8 shows the time-series  $V_p$   
555 and  $V_s$  inverted values extracted from this surface layer, alongside calculated  
556 effective rainfall, soil moisture data from a cosmic-ray sensor measuring shallow  
557 ( $\sim 0.1$  m bgl) moisture content across the site.  $V_p$  increases and decreases in  
558 relation to soil moisture, but with a slight time lag. The lag effect is caused by  
559 the difference of the sampling depth of the moisture sensor ( $< 0.1$  m bgl) and the  
560 depth of the  $V_p$  readings (2 - 4 m bgl); the moisture content of the HHLO near-  
561 surface changes more quickly in relation to net infiltration and  
562 evapotranspiration rates (shown by the hourly soil moisture, faint green line)  
563 than the top 2 - 4 m of the landslide, which will be less subject to  
564 evapotranspiration processes at depth. It is also worth noting that inverted  
565 velocities will be smoothed values from the true velocities, due to the spatial and  
566 temporal smoothness constraints used.

567 Furthermore, the calculated  $V_p/V_s$  ratio (Figure 7f), which is an indicator of  
568 material saturation (Uyanik, 2011), better reflects changes in moisture content in  
569 Figure 8. Crucially, the minimum  $V_p$  (350 m/s) in the time-series is 24% less than  
570 the maximum  $V_p$  (462 m/s). Given that topographic effects alone can cause  
571 variations in  $V_p > \pm 10\%$  (Figure 6), the changes in seismic velocity over time  
572 could easily be masked if the data are not processed correctly. This  
573 demonstrates the necessity for including accurate topography in long-term SRT  
574 monitoring campaigns in landslide settings.



575

576 Figure 8: The top panel shows variation in bulk  $V_p$  and  $V_s$  readings from the sliding layer at the  
 577 HHLO (see Figure 7 for location of this layer). The shaded areas are the 1<sup>st</sup> and 3<sup>rd</sup> quartiles of the  
 578 range in  $V_p$  and  $V_s$ . The  $V_p/V_s$  ratio, derived from the bulk  $V_p$  and  $V_s$  readings is shown. In the  
 579 bottom panel, weekly effective rainfall, showing periods of net infiltration/evapotranspiration at the  
 580 HHLO, and soil moisture from a surface sensor measuring to <0.1m bgl. The variation in  $V_p$  broadly  
 581 follows the increases and decreases in moisture content, while  $V_s$  shows little variation. The derived  
 582  $V_p/V_s$  ratio shows greatest sensitivity to the moisture content of the surface sliding layer at HHLO.

## 583 6. Conclusions

584 SRT is rarely used for the long-term assessment of landslides prone to  
 585 hydrological destabilization, but has great potential for high-resolution spatial  
 586 monitoring. This is particularly the case in slopes with high spatial heterogeneity  
 587 in which monitoring data obtained from sparse point observations is insufficient  
 588 to capture the complexity of the landslide system. Landslide monitoring  
 589 campaigns using SRT can determine seismic attributes of slipped materials,  
 590 which provides information on elastic property changes due to temporal  
 591 variations in moisture content. However, failing to give due attention to the  
 592 possible sources of error in SRT surveys can lead to artefacts in the time-lapse  
 593 data, which can easily mask changes arising from genuine variations in the  
 594 elastic properties of landslide materials, including the underlying rock. In this  
 595 study, we provide a workflow for addressing the errors associated with producing



596 a reliable time-series of inverted seismic velocity models, and have shown how  
597 velocities in the near-surface soil layers are sensitive to variations in moisture  
598 content.

599 Standard approaches to quality assessment and processing of SRT data aid in  
600 minimizing individual survey data error. The use of emerging methods to  
601 increase picking accuracy, such as automatic detection algorithms, machine  
602 learning and statistical approaches will also decrease data errors introduced in to  
603 the creation of time-lapse data from standalone surveys. In this study, data from  
604 each survey were processed using reciprocal error analysis to ensure  $e < 5\%$  of  
605 travel-time for all datasets. However, in the case of producing time-lapse data  
606 from these individual datasets, we underscore the importance of using detailed,  
607 unique topography data for processing each time-step. This crucial step could  
608 easily be overlooked by inaccurate assumptions regarding field setup, receiver  
609 spacing landslide surface movement between surveys, even by experienced SRT  
610 operators.

611 For the data considered here, changes in topography lead to  $> \pm 10\%$  variations  
612 in apparent seismic velocities in 23% of the data for the unconsolidated near-  
613 surface. Our data exhibits a 24% difference between the fastest and slowest  $V_p$   
614 observed in this layer, caused by variations in elastic properties induced by  
615 changes in moisture content, underscoring the need to properly account for  
616 topography effects. To avoid the errors associated with changes in topography,  
617 accurate source-receiver positions are important when processing SRT  
618 monitoring data. Several other steps, including the repositioning of receivers in  
619 the field, the use of data quality indicators (such as travel-time reciprocity) and  
620 robust reference models for inversion further reduces these errors. If these  
621 potential sources of error are managed correctly, SRT presents a useful tool for  
622 the identification of heterogeneous subsurface conditions and their changing  
623 properties over time in active landslide settings.

## 624 **Acknowledgements**

625 The authors would like to acknowledge Florian Wagner for advice on the *pyGIMLi*  
626 API. We would also like to acknowledge members, students and visiting scholars  
627 of the BGS' Geophysical Tomography team for their input and support. We would  
628 like to thank Josie Gibson, Frances Standen and James Standen for their  
629 continued support of our monitoring activities at Hollin Hill. This work was funded  
630 by a NERC GW4+ UK Doctoral Training Partnership Studentship (Grant

631 NE/L002434/1) and in part by the BGS University Funding Initiative (S337), which  
632 are gratefully acknowledged. Jim Whiteley, Jonathan Chambers, Jimmy Boyd,  
633 Mihai Cimpoiasu, Jessica Holmes, Cornelia Inauen, Arnaud Watlet, Luke Hawley-  
634 Sibbett and Russell Swift publish with the permission of the Executive Director,  
635 British Geological Survey (UKRI-NERC). All content generated as part of this work  
636 is copyright of British Geological Survey © UKRI 2020/ The University of Bristol  
637 2020.

638

### 639 **References**

- 640 Angeli, M.-G., Pasuto, A. & Silvano, S. 2000. A critical review of landslide  
641 monitoring experiences. *Engineering Geology*, 55, 133-147.
- 642 Bhowmick, S. 2017. Role of Vp/Vs and Poisson's Ratio in the Assessment of  
643 Foundation(s) for Important Civil Structure(s). *Geotechnical and Geological*  
644 *Engineering*, 35, 527-534.
- 645 Bièvre, G., Jongmans, D., Winiarski, T. & Zumbo, V. 2012. Application of  
646 geophysical measurements for assessing the role of fissures in water  
647 infiltration within a clay landslide (Trièves area, French Alps). *Hydrological*  
648 *Processes*, 26, 2128-2142.
- 649 Biot, M. A. 1956. Theory of Propagation of Elastic Waves in a Fluid-Saturated  
650 Porous Solid. I. Low-Frequency Range. *The Journal of the Acoustical*  
651 *Society of America*, 28, 168-178.
- 652 Chambers, J. E., Wilkinson, P. B., Kuras, O., Ford, J. R., Gunn, D. A., Meldrum, P. I.,  
653 Pennington, C. V. L., Weller, A. L., Hobbs, P. R. N. & Ogilvy, R. D. 2011.  
654 Three-dimensional geophysical anatomy of an active landslide in Lias  
655 Group mudrocks, Cleveland Basin, UK. *Geomorphology*, 125, 472-484.
- 656 Dangeard, M., Bodet, L., Pasquet, S., Thiesson, J., Guérin, R., Jougnot, D. &  
657 Longuevergne, L. 2018. Estimating picking errors in near-surface seismic  
658 data to enable their time-lapse interpretation of hydrosystems. *Near*  
659 *Surface Geophysics*, 16, 613-625.
- 660 Dashwood, B., Gunn, D., Curioni, G., Inauen, C., Swift, R., Chapman, D., Royal, A.,  
661 Hobbs, P., Reeves, H. & Taxil, J. 2019. Surface wave surveys for imaging  
662 ground property changes due to a leaking water pipe. *Journal of Applied*  
663 *Geophysics*, 103923.

- 664 Flammer, I., Blum, A., Leiser, A. & Germann, P. 2001. Acoustic assessment of  
665 flow patterns in unsaturated soil. *Journal of Applied Geophysics*, 46, 115-  
666 128.
- 667 Gassmann, F. 1951. *Über die Elastizität Poröser Medien*.
- 668 Grandjean, G., Hibert, C., Mathieu, F., Garel, E. & Malet, J.-P. 2009. Monitoring  
669 water flow in a clay-shale hillslope from geophysical data fusion based on  
670 a fuzzy logic approach. *Comptes Rendus Geoscience*, 341, 937-948.
- 671 Intrieri, E., Gigli, G., Mugnai, F., Fanti, R. & Casagli, N. 2012. Design and  
672 implementation of a landslide early warning system. *Engineering Geology*,  
673 147, 124-136.
- 674 Jaboyedoff, M., Del Gaudio, V., Derron, M.-H., Grandjean, G. & Jongmans, D.  
675 2019. Characterizing and monitoring landslide processes using remote  
676 sensing and geophysics. *Engineering Geology*, 105167.
- 677 Khalaf, A., Camerlynck, C., Florsch, N. & Schneider, A. 2018. Development of an  
678 adaptive multi-method algorithm for automatic picking of first arrival  
679 times: application to near surface seismic data. *Near Surface Geophysics*,  
680 16, 507-526.
- 681 Lu, Z. & Sabatier, J. M. 2009. Effects of Soil Water Potential and Moisture Content  
682 on Sound Speed. *Soil Science Society of America Journal*, 73, 1614-1625.
- 683 Lucas, D. R., Fankhauser, K. & Springman, S. M. 2017. Application of  
684 geotechnical and geophysical field measurements in an active alpine  
685 environment. *Engineering Geology*, 219, 32-51.
- 686 Merritt, A. J., Chambers, J. E., Murphy, W., Wilkinson, P. B., West, L. J., Gunn, D.  
687 A., Meldrum, P. I., Kirkham, M. & Dixon, N. 2013. 3D ground model  
688 development for an active landslide in Lias mudrocks using geophysical,  
689 remote sensing and geotechnical methods. *Landslides*, 11, 537-550.
- 690 Pasquet, S., Bodet, L., Bergamo, P., Guérin, R., Martin, R., Mourgues, R. &  
691 Tournat, V. 2016a. Small-Scale Seismic Monitoring of Varying Water Levels  
692 in Granular Media. *Vadose Zone Journal*, 15.
- 693 Pasquet, S., Holbrook, W. S., Carr, B. J. & Sims, K. W. W. 2016b. Geophysical  
694 imaging of shallow degassing in a Yellowstone hydrothermal system.  
695 *Geophysical Research Letters*, 43, 12,027-12,035.
- 696 Perrone, A., Lapenna, V. & Piscitelli, S. 2014. Electrical resistivity tomography  
697 technique for landslide investigation: A review. *Earth-Science Reviews*,  
698 135, 65-82.

- 699 Romero-Ruiz, A., Linde, N., Keller, T. & Or, D. 2018. A Review of Geophysical  
700 Methods for Soil Structure Characterization. *Reviews of Geophysics*, 56,  
701 672-697.
- 702 Rücker, C., Günther, T. & Wagner, F. M. 2017. pyGIMLi: An open-source library for  
703 modelling and inversion in geophysics. *Computers & Geosciences*, 109,  
704 106-123.
- 705 Uhlemann, S., Chambers, J., Wilkinson, P., Maurer, H., Merritt, A., Meldrum, P.,  
706 Kuras, O., Gunn, D., Smith, A. & Dijkstra, T. 2017. Four-dimensional  
707 imaging of moisture dynamics during landslide reactivation. *Journal of*  
708 *Geophysical Research: Earth Surface*, 122, 398-418.
- 709 Uhlemann, S., Hagedorn, S., Dashwood, B., Maurer, H., Gunn, D., Dijkstra, T. &  
710 Chambers, J. 2016. Landslide characterization using P- and S-wave seismic  
711 refraction tomography — The importance of elastic moduli. *Journal of*  
712 *Applied Geophysics*, 134, 64-76.
- 713 Uyanik, O. 2011. The porosity of saturated shallow sediments from seismic  
714 compressional and shear wave velocities. *Journal of Applied Geophysics*,  
715 73, 16-24.
- 716 Walter, M., Arnhardt, C. & Joswig, M. 2012. Seismic monitoring of rockfalls, slide  
717 quakes, and fissure development at the Super-Sauze mudslide, French  
718 Alps. *Engineering Geology*, 128, 12-22.
- 719 Whiteley, J. S., Chambers, J. E., Uhlemann, S., Wilkinson, P. B. & Kendall, J. M.  
720 2019. Geophysical Monitoring of Moisture-Induced Landslides: A Review.  
721 *Reviews of Geophysics*, 57, 106-145.
- 722 Wyllie, M. R. J., Gregory, A. R. & Gardner, L. W. 1956. Elastic wave velocities in  
723 heterogeneous and porous media. *Geophysics*, 21, 41-70.

724

725

726 **Appendix**  
727

<b>P-wave inversions</b>																
<b>Starting model</b>	Velocity gradient model (see Table 2 for values)															
<b>Time-step</b>	<b>0</b>	<b>1</b>	<b>2</b>	<b>3</b>	<b>4</b>	<b>5</b>	<b>6</b>	<b>7</b>	<b>8</b>	<b>9</b>	<b>10</b>	<b>11</b>	<b>12</b>	<b>13</b>	<b>14</b>	<b>15</b>
<b><math>\chi^2</math></b>	0.98 2	1.49 5	1.95 2	1.34 5	1.47 8	1.13 8	1.43 4	1.35 8	1.84 8	1.57 3	1.28 8	1.31 6	1.25 8	0.98 2	1.15 7	0.99 2
<b>RMS</b>	2.97 0	3.78 8	4.97 1	4.31 0	4.14 3	4.41 2	4.72 1	5.24 4	5.71 3	5.43 1	4.01 0	3.96 5	3.72 7	3.40 4	4.15 7	3.49 2
<b><math>\chi^2</math> divergence</b>	0.01 8	0.49 5	0.95 2	0.34 5	0.47 8	0.13 8	0.43 4	0.35 8	0.84 8	0.57 3	0.28 8	0.31 6	0.25 8	0.01 8	0.15 7	0.00 8
<b>Starting model</b>	Reference model derived from results of first stage inversion (i.e., time-step 15)															
<b>Time-step</b>	<b>0</b>	<b>1</b>	<b>2</b>	<b>3</b>	<b>4</b>	<b>5</b>	<b>6</b>	<b>7</b>	<b>8</b>	<b>9</b>	<b>10</b>	<b>11</b>	<b>12</b>	<b>13</b>	<b>14</b>	<b>15</b>
<b><math>\chi^2</math></b>	0.98 4	1.51 6	1.90 4	1.48 6	1.59 3	1.44 0	1.73 3	1.44 5	2.23 8	1.89 3	1.44 2	1.35 1	1.35 7	1.16 1	1.33 0	0.92 7
<b>RMS</b>	3.15 7	3.93 5	4.86 0	4.46 6	4.06 9	5.04 4	4.72 9	5.20 2	5.69 3	5.51 5	4.31 4	3.96 6	4.05 0	3.98 7	4.14 8	3.38 5
<b><math>\chi^2</math> divergence</b>	0.01 6	0.51 6	0.90 4	0.48 6	0.59 3	0.44 0	0.73 3	0.44 5	1.23 8	0.89 3	0.44 2	0.35 1	0.35 7	0.16 1	0.33 0	0.07 3
<b>S-wave inversions</b>																
<b>Starting model</b>	Velocity gradient model (see Table 2 for values)															
<b>Time-step</b>	<b>0</b>	<b>1</b>	<b>2</b>	<b>3</b>	<b>4</b>	<b>5</b>	<b>6</b>	<b>7</b>	<b>8</b>	<b>9</b>	<b>10</b>	<b>11</b>	<b>12</b>	<b>13</b>	<b>14</b>	<b>15</b>
<b><math>\chi^2</math></b>	1.11 7	1.41 6	2.06 1	1.95 9	2.65 4	1.99 1	2.49 9	1.56 3	1.77 1	3.82 2	1.61 4	2.87 3	2.51 7	1.91 0	2.17 9	2.10 0
<b>RMS</b>	1.20 6	1.41 5	1.76 4	1.67 8	2.00 1	1.68 5	1.91 0	1.49 1	1.70 4	1.97 4	1.71 6	2.06 8	1.93 3	1.62 9	1.77 0	1.75 0
<b><math>\chi^2</math> divergence</b>	0.11 7	0.41 6	1.06 1	0.95 9	1.65 4	0.99 1	1.49 9	0.56 3	0.77 1	2.82 2	0.61 4	1.87 3	1.51 7	0.91 0	1.17 9	1.10 0
<b>Starting model</b>	Reference model derived from results of first stage inversion (i.e., time-step 0)															
<b>Time-step</b>	<b>0</b>	<b>1</b>	<b>2</b>	<b>3</b>	<b>4</b>	<b>5</b>	<b>6</b>	<b>7</b>	<b>8</b>	<b>9</b>	<b>10</b>	<b>11</b>	<b>12</b>	<b>13</b>	<b>14</b>	<b>15</b>
<b><math>\chi^2</math></b>	0.99 0	1.52 0	2.08 2	1.98 8	2.62 9	1.91 2	2.24 3	1.71 3	1.68 1	1.72 8	1.81 2	2.86 1	2.53 3	1.91 3	2.04 7	2.03 9
<b>RMS</b>	1.12 4	1.47 9	1.65 7	1.74 5	2.01 8	1.53 2	1.82 0	1.73 1	1.72 4	1.71 6	2.34 9	2.10 6	2.07 4	1.61 2	1.88 9	1.67 5
<b><math>\chi^2</math> divergence</b>	0.01 0	0.52 0	1.08 2	0.98 8	1.62 9	0.91 2	1.24 3	0.71 3	0.68 1	0.72 8	0.81 2	1.86 1	1.53 3	0.91 3	1.04 7	1.03 9

728 *Table 3: The results of the two-stage inversion process for both the Vp and Vs surveys. In stage*  
 729 *one, a velocity gradient model with the parameters in Table 2 is used to perform stand-alone*  
 730 *inversions of each time-step. The 'best' result (highlighted green) is then assessed by looking at*  
 731 *divergence from a perfect model fit (i.e., a normalised  $\chi^2$  value, or ' $\chi^2$  divergence'). The 'best'*  
 732 *model is then used as a 'reference model' for the second stage inversion. The 'reference model' is*  
 733 *used for the inversion of each time-step in the second stage inversion, providing a real-world,*  
 734 *common starting model for the time-series.*